Dual Matrix Converter Based Wireless Power Transfer System

Xin Felix Chen, *Graduate Student Member, IEEE*, Chi K. Tse, *Fellow, IEEE*, C. Q. Jiang, *Senior Member, IEEE*, Qianhong Chen, *Member, IEEE*, and Ching-Ming Lai, *Senior Member, IEEE*

***Abstract*—This article introduces a dual matrix converter-based wireless power transfer system for three-phase loads. The proposed system enables direct ac–ac power conversion, eliminating the need for bulky and short-lifetime electrolytic capacitors, thereby enhancing power density and reliability. In addition, the article explores modulation strategies for the proposed structure. Various modulation waveforms are compared and analyzed, revealing that antisymmetric and periodic flip modulations can mitigate phase-shift effects on the system's total harmonic distortion (THD) performance, maintaining stable THD levels over a wide load range. Through Fourier analysis, it is observed that the fundamental components of antisymmetric and periodic flip waveforms are symmetric during a switching period. Leveraging this symmetry, an improved dwell time calculation method is proposed to reduce THD values for both grid-side and load-side currents. Finally, a prototype is constructed to validate the theoretical analysis, achieving a maximum efficiency of 93.3% and a minimum THD of 1.11%.**

***Index Terms*—Matrix converter (MC), modulation strategy, three-phase load, wireless power transfer (WPT).**

I. Introduction

WIRELESS power transfer (WPT) techniques have seen significant advancement over the past few decades. Previous research has primarily concentrated on battery loads [1], [2], where the WPT system typically provides a single-phase output. However, many practical applications involve three-phase loads, such as electric motors. Consequently, wireless motor drive systems have been proposed to cater to these types of loads [3]. Compared to conventional WPT systems, wireless motor drive systems typically incorporate additional inverters for motor control. This multiple power conversion process can lead to increased losses, as well as larger system volumes and weights [4], [5], [6]. Therefore, integration has become a crucial design consideration for wireless motor drive systems. Specifically, combining the WPT rectifier and the motor drive inverter allows for simultaneous power transfer and motor control.

Integration can be primarily achieved through multicoil-based methods [7], [8], [9], [10] and matrix converter (MC)-based methods [11], [12], [13], [14], [15], [16], [17], [18], [19], [20], [21], [22], [23]. For multicoil-based methods, magnetic coupler coils are designed to match the number of motor phases. In addition, extra resonant branches are required in each coil set for independent control of different motor phases. This configuration can eliminate the need for motor drive inverters and improve system robustness. However, the extensive use of passive components may reduce system power density. Furthermore, the multicoil structure is limited to motors with trapezoidal electromotive force (EMF), such as switched reluctance motors [7], [8], [9] or stepper motors [10].

MC-based methods offer an alternative approach, providing direct ac–ac conversion without the need for intermediate dc stages. This can enhance system efficiency and reduce the overall size and weight of the system. The MC can be either single-phase (1 ph) [11], [12], [13], [14], [15] or three-phase (3 ph) [16], [17], [18], [19], [20], [21], [22], [23], depending on the motor types. It is important to note that the single-phase output for motor loads differs from that for battery loads, with an ac output for motors and a dc output for batteries. The single-phase MC can be further classified into half-bridge [11], [12] and full-bridge structures [13], [14], [15], as shown in Fig. 1(a) and (b), respectively.

The three-phase MC primarily exists in two forms: three-phase half-wave structures [16], [17] and three-phase bridge structures [18], [19], [20], [21], [22], as shown in Fig. 1(c) and (d), respectively. The half-wave structure is suitable for three-phase four-wire connections, while the bridge structure is compatible with three-phase three-wire connections. The bridge structure offers higher voltage utilization and lower voltage ripples compared to the half-wave structure but requires more switching devices. To reduce the number of switching devices, common-source connected MOSFETs can be replaced with reverse-connected MOSFETs and diodes [23], as shown in Fig. 1(e). However, this simplified structure only allows current to flow in single directions and transfers only positive voltages to the resonant tank. These limitations increase the risk of

Received 9 February 2025; revised 5 June 2025; accepted 27 July 2025. Date of publication 1 August 2025; date of current version 8 September 2025. This work was supported by the Hong Kong RGC Theme-Based Research Scheme Project under Grant T23-701/20R and Grant NSFC/RGC Joint Research Scheme N_CityU 124/24. Recommended for publication by Associate Editor N. R. Zargari. *(Corresponding author: Chi K. Tse.)*

Xin Felix Chen, Chi K. Tse, and C. Q. Jiang are with the Department of Electrical Engineering, City University of Hong Kong, Hong Kong SAR, China (e-mail: xchen994-c@my.cityu.edu.hk; chitse@cityu.edu.hk; chjiang@cityu.edu.hk).

Qianhong Chen is with the Aero-Power Sci-Tech Center, Nanjing University of Aeronautics and Astronautics, Nanjing 210016, China (e-mail: chenqh@nuaa.edu.cn).

Ching-Ming Lai is with the Department of Electrical Engineering, National Chung Hsing University, Taichung 402, Taiwan (e-mail: pecmlai@nchu.edu.tw).

Color versions of one or more figures in this article are available at https://doi.org/10.1109/TPEL.2025.3594719.

Digital Object Identifier 10.1109/TPEL.2025.3594719

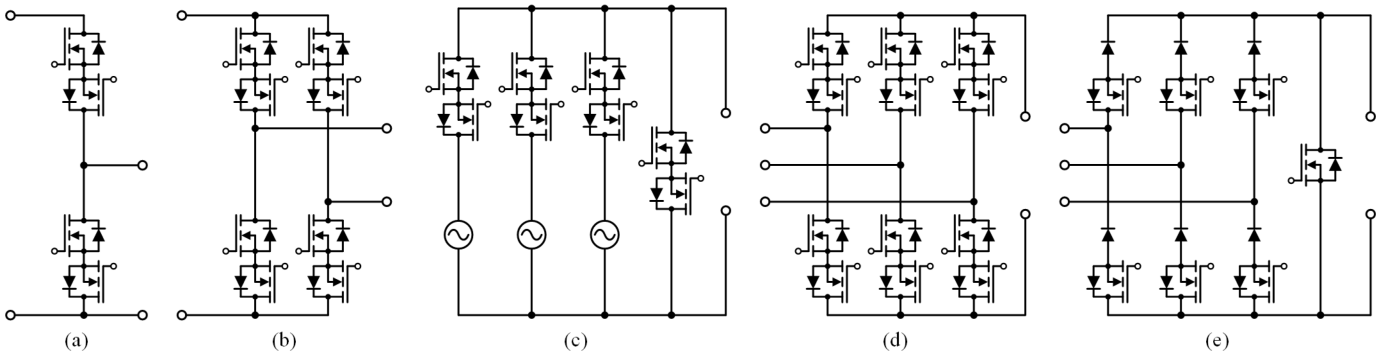

Fig. 1. MCs for WPT systems. (a) Single-phase half-bridge structure. (b) Single-phase full-bridge structure. (c) Three-phase half-wave structure. (d) Three-phase bridge structure. (e) Three-phase simplified bridge structure.

overvoltage damage and reduce the system's power capacity. In addition, there are various other types of MCs, such as indirect and sparse structures [24], [25]. Since these structures have not yet been applied in WPT systems, they are omitted in this discussion and can be explored in future studies.

When comparing a MC-based system with a multicoil-based system, the former may be less reliable due to the fragility of semiconductor devices. However, the MC system can significantly improve power density by utilizing semiconductor devices and eliminating bulky electrolytic capacitors [24], [25]. Moreover, employing suitable modulation techniques can extend the MC system to motors with sinusoidal EMF.

The modulation techniques for MCs can be categorized into pulse density modulation (PDM) [11], [15], [23] and space vector modulation (SVM) [18], [19], [20], [21], [22]. PDM regulates the high-frequency pulse density to match the magnitude of the low-frequency ac waveform, enabling zero current switching. However, to minimize harmonics in motor windings, a significantly higher switching frequency is required to reduce tracking errors. Conversely, the SVM technique adjusts the conduction time of different output phases during each switching period. Although it involves more switching actions, SVM can significantly reduce harmonics compared to PDM at the same switching frequency. However, calculating dwell time is complicated for SVM, as the reference vectors vary with the sinusoidal resonant voltage or current within a switching period.

Overall, this article focuses on integrating MCs into WPT systems, specifically targeting three-phase load applications. Inspired by previous studies that utilized MCs on the load side [12], [18], this article extends their use to both the grid and load sides. Given the common use of three-phase three-wire configurations for grid and motor connections, this article illustrates the application using a three-phase bridge MC. Furthermore, the switching frequency for a WPT system is typically tuned around 85 kHz [26]. Given this relatively low switching frequency, the SVM technique is adopted here to achieve desirable total harmonic distortion (THD) performance. Building on existing SVM strategies [18], [19], [20], [21], [22], this research examines various modulation waveforms and recalculates the dwell time to maintain low THD over a wide load range. Notably, the focus is on rotational applications, where coupler parameters remain relatively stable during operation [27], [28]. Therefore, the issue of misalignment is not addressed in this study.

The rest of this article is organized as follows. Section II introduces the system's structure and provides basic working principles of the system. Section III discusses the modulation strategy of the proposed system, including a comparison of different modulation waveforms and the derivation of improved dwell time. Section IV presents the simulation and experimental results. Finally, Section V concludes this article.

II. System Description

A dual MC-based WPT system is shown in Fig. 2, which is composed of a three-phase input filter (L_f, C_f), a primary-side three-phase bridge MC ($\mathrm{Q_1}$–$\mathrm{Q_6}$), a resonant tank (L_P, L_S, C_P, C_S, R_P, R_S), a secondary-side three-phase bridge MC ($\mathrm{S_1}$–$\mathrm{S_6}$), a three-phase output filter (C'_f), and a three-phase load (L'_f, R_L).

As shown in Fig. 2, the major difference between the conventional structure and the proposed structure is that ac–dc–ac conversion configurations are replaced with MCs on both grid and load sides. Correspondingly, the filter types need to be adjusted. For example, the CL-type grid filter in the conventional structure changes to the *LC*-type filter in the proposed structure.

In addition, the absence of an intermediate power stage in the MC eliminates the need for electrolytic capacitors (C_in, C_o). Notably, capacitors C_f and C'_f mainly serve as filters with significantly lower capacitance values than storage capacitors. As a result, film capacitors with high reliability can be utilized.

A. Matrix Converter

The grid-side MC converts input three-phase low-frequency ac power directly into single-phase high-frequency ac power for the resonant tank. Similarly, the load-side MC converts the single-phase high-frequency ac power of the resonant tank directly into three-phase low-frequency ac power for three-phase loads. Note that the grid-side and load-side MCs are symmetric. Thus, an additional advantage of the proposed structure is the ability for bidirectional power flow.

In both MCs, each four-quadrant switch set comprises two MOSFETs in a common-source connection. For example, $\mathrm{Q_1}$ is composed of $\mathrm{Q_{11}}$ and $\mathrm{Q_{21}}$, while $\mathrm{S_5}$ is composed of $\mathrm{S_{15}}$ and $\mathrm{S_{25}}$,

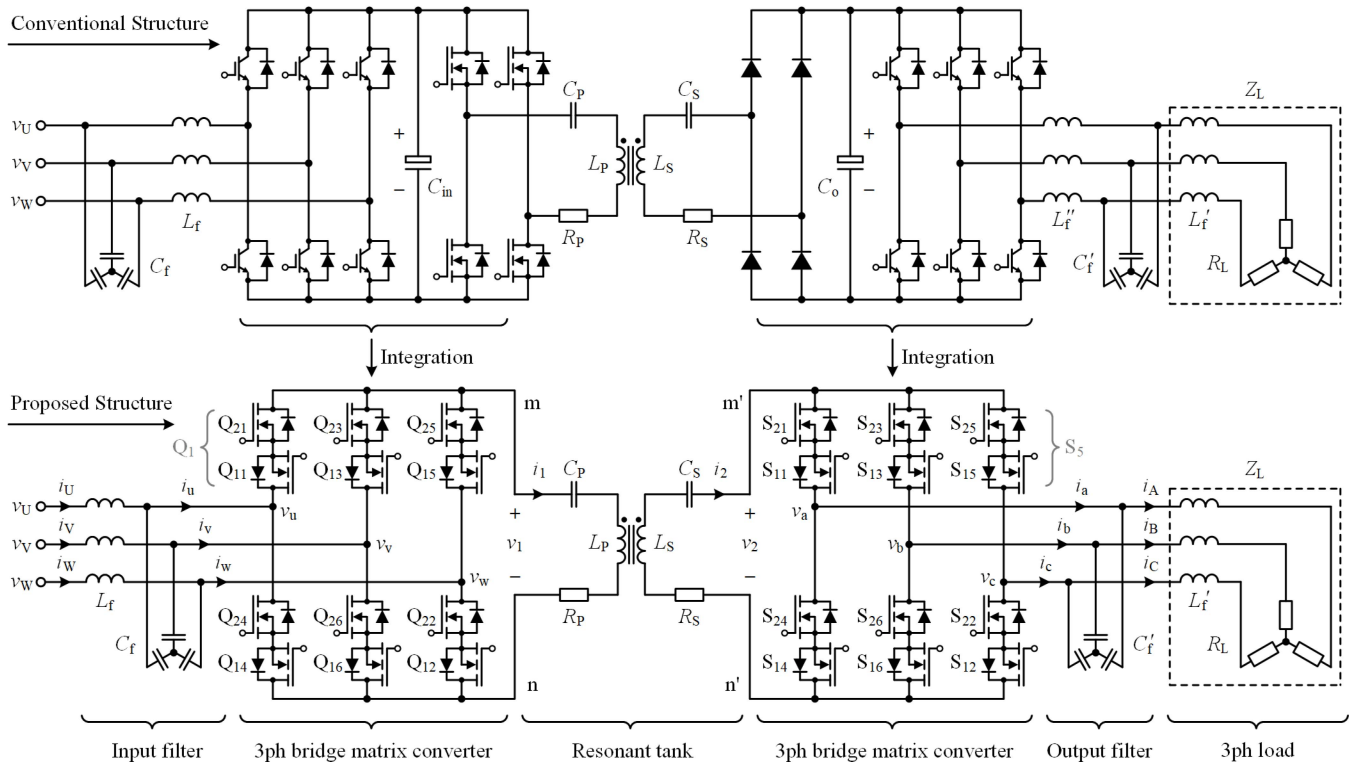

Fig. 2. Dual MC-based WPT system.

as shown in Fig. 2. Due to the use of four-quadrant switching devices, there are no freewheeling paths for the resonant current to close itself during the commutation transition. Therefore, a diode snubber circuit [21], [25] is used for each MC in this article.

Moreover, both short-circuit and open-circuit conditions should be prevented. Thus, only two switching devices in each MC conduct at any time instant, one in the upper half of the bridge (Q_1, Q_3, Q_5 or S_1, S_3, S_5), and the other in the lower half (Q_4, Q_6, Q_2 or S_4, S_6, S_2). Then, the following constraint needs to be met:

$$\begin{cases} s_{\mathrm{um}} + s_{\mathrm{vm}} + s_{\mathrm{wm}} = 1,\ s_{\mathrm{un}} + s_{\mathrm{vn}} + s_{\mathrm{wn}} = 1 \\ s_{\mathrm{am'}} + s_{\mathrm{bm'}} + s_{\mathrm{cm'}} = 1,\ s_{\mathrm{an'}} + s_{\mathrm{bn'}} + s_{\mathrm{cn'}} = 1 \end{cases} \tag{1}$$

where the switching function is defined as

$$s_{ij} = \begin{cases} 1 & \text{ON} \\ 0 & \text{OFF.} \end{cases} i \in \{\mathrm{u}, \mathrm{v}, \mathrm{w}, \mathrm{a}, \mathrm{b}, \mathrm{c}\}; j \in \{\mathrm{m}, \mathrm{n}, \mathrm{m}', \mathrm{n}'\}. \tag{2}$$

B. Compensation Topology

Both series–series (S/S) and LCC/LCC compensation networks are applicable to the dual MC-based WPT system. For simplicity, this article takes the S/S compensation as an example.

In Fig. 2, L_{P} and L_{S} are primary and secondary-side self-inductance, while C_{P} and C_{S} are primary and secondary-side compensation capacitance. Besides, R_{P} and R_{S} represent the total parasitic resistance of the coupler coils and compensation capacitors. Based on the fundamental harmonic approximation method, a basic relationship of S/S compensation can be obtained by

$$\begin{cases} \dot{V}_1 = Z_{\mathrm{P}}\dot{I}_1 - \mathrm{j}\omega_{\mathrm{s}} M \dot{I}_2 \\ \dot{V}_2 = \mathrm{j}\omega_{\mathrm{s}} M \dot{I}_1 - Z_{\mathrm{S}}\dot{I}_2 \end{cases} \tag{3}$$

where $\omega_{\mathrm{s}} = 2\pi f_{\mathrm{s}}$ is the angular switching frequency; $\dot{V}_1$, $\dot{V}_2$, $\dot{I}_1$, and $\dot{I}_2$ denote the fundamental component vectors of v_1, v_2, i_1, and i_2, respectively. Moreover, Z_{P} and Z_{S} are defined as

$$Z_{\mathrm{P}} = \mathrm{j}\omega_{\mathrm{s}} L_{\mathrm{P}} + \frac{1}{\mathrm{j}\omega_{\mathrm{s}} C_{\mathrm{P}}} + R_{\mathrm{P}},\ Z_{\mathrm{S}} = \mathrm{j}\omega_{\mathrm{s}} L_{\mathrm{S}} + \frac{1}{\mathrm{j}\omega_{\mathrm{s}} C_{\mathrm{S}}} + R_{\mathrm{S}}. \tag{4}$$

Solving (3), we can derive the primary- and secondary-side resonant currents $\dot{I}_1$ and $\dot{I}_2$ as follows:

$$\dot{I}_1 = \frac{Z_{\mathrm{S}}\dot{V}_1 - \mathrm{j}\omega_{\mathrm{s}} M \dot{V}_2}{(\omega_{\mathrm{s}} M)^2 + Z_{\mathrm{P}} Z_{\mathrm{S}}},\ \dot{I}_2 = \frac{\mathrm{j}\omega_{\mathrm{s}} M \dot{V}_1 - Z_{\mathrm{P}}\dot{V}_2}{(\omega_{\mathrm{s}} M)^2 + Z_{\mathrm{P}} Z_{\mathrm{S}}}. \tag{5}$$

For S/S compensation, the switching frequency ω_{s} is normally set close to the resonant frequency, i.e.,

$$\omega_0 = 2\pi f_0 = \frac{1}{\sqrt{L_{\mathrm{P}} C_{\mathrm{P}}}} = \frac{1}{\sqrt{L_{\mathrm{S}} C_{\mathrm{S}}}}. \tag{6}$$

Besides, supposing the phase angle of v_1 is zero and denoting the phase difference between v_1 and v_2 as θ_{PS} (as shown in Fig. 3), the primary- and secondary-side resonant voltages $\dot{V}_1$ and $\dot{V}_2$ can be expressed as

$$\dot{V}_1 = V_1,\ \dot{V}_2 = V_2 \angle \theta_{\mathrm{PS}}. \tag{7}$$

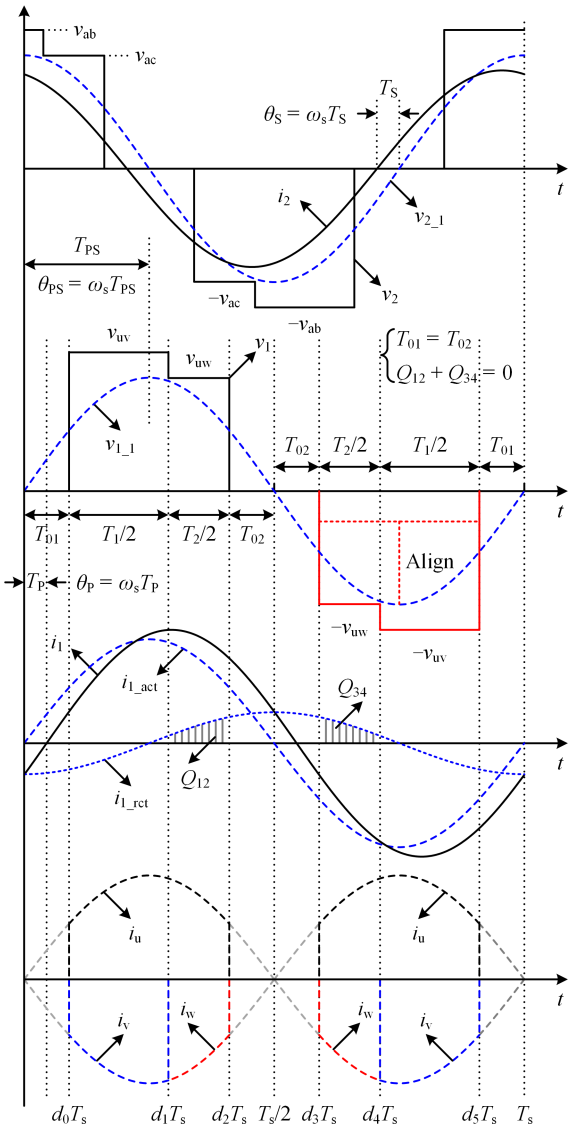

Fig. 3. Antisymmetric modulation waveforms in sector I.

Combining (3)–(7), the primary- and secondary-side complex power can be obtained as

$$\begin{cases} \tilde{S}_1 = \dot{V}_1 \cdot \dot{I}_1^* = P_1 + \mathrm{j}Q_1 = \dfrac{R_S V_1^2 + \Delta_1}{\Delta_3} + \mathrm{j}\dfrac{\Delta_2}{\Delta_3} \\ \tilde{S}_2 = \dot{V}_2 \cdot \dot{I}_2^* = P_2 + \mathrm{j}Q_2 = \dfrac{-R_P V_2^2 + \Delta_1}{\Delta_3} - \mathrm{j}\dfrac{\Delta_2}{\Delta_3} \end{cases} \tag{8}$$

where

$$\begin{cases} \Delta_1 = \omega_0 M V_1 V_2 \sin\theta_{PS} \\ \Delta_2 = \omega_0 M V_1 V_2 \cos\theta_{PS} \\ \Delta_3 = (\omega_0 M)^2 + R_P R_S. \end{cases} \tag{9}$$

From (8), it is seen that $\theta_{PS} = \pm 90^\circ$ ($\Delta_2 = 0$) needs to be satisfied to eliminate reactive power in the resonant tank. Besides, if $\theta_{PS} > 0$, we can have $|P_1| > |P_2|$, then the power is transferred from the primary side to the secondary side. Conversely, for $\theta_{PS} < 0$, with $|P_1| < |P_2|$, the power is transferred from the secondary side to the primary side.

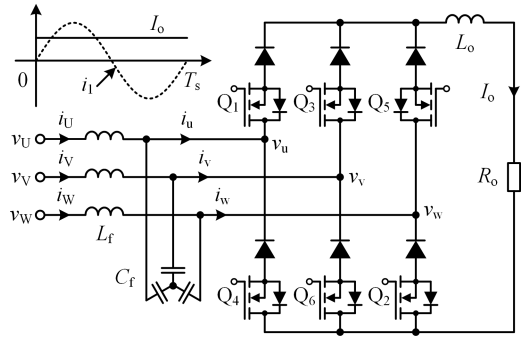

Fig. 4. Structure of the current source converter.

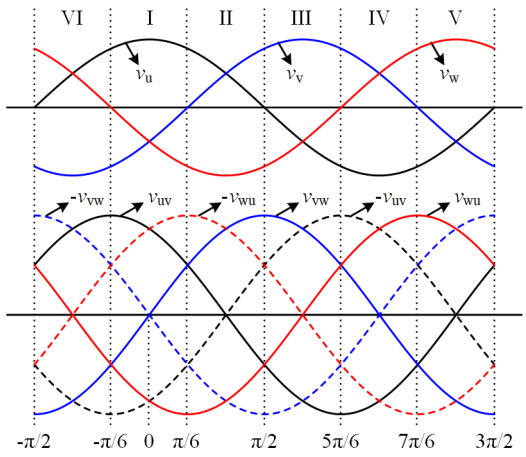

Fig. 5. Grid-side waveforms and sector division.

This article focuses on the power flow from the grid side to the load side, and the system has a maximum output power at $\theta_{PS} = 90^\circ$. In this case, the phase angles of θ_P and θ_S are approximately zero. With the decrease of θ_{PS}, the output power also decreases, while θ_P and θ_S increase. For an intuitive illustration, we consider $\theta_{PS} = 90^\circ$ as the initial operating point and introduce the complementary angle of θ_{PS} (denoted as θ'_{PS}) to represent the phase shift.

III. Modulation Strategy

For the dual MC-based WPT system, this section will discuss its modulation strategy. The waveforms and space vectors of the grid-side and load-side MCs are similar due to the symmetric structure. For brevity, the grid-side MC is used for illustration in this section.

A. Limitations of Conventional SVM

The conventional SVM is initially applied for the current source converter shown in Fig. 4 [29]. To implement SVM, the three-phase voltages are usually divided into six sectors, as shown in Fig. 5. In each sector, the top two highest line voltages will be used to maximize voltage utilization for power transmission. For example, in sector I, voltages v_{uv} and $-v_{wu}$ are used.

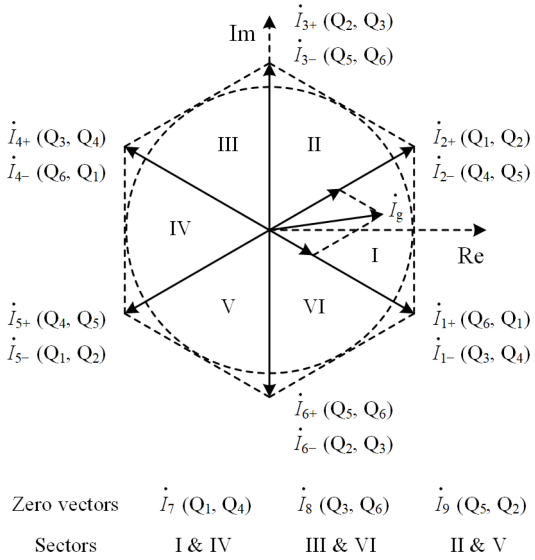

Fig. 6. Space current vectors of MCs.

Based on the sector division in Fig. 5, the space vectors of the current source converter are provided in Fig. 6. There are a total of nine current vectors, including six active vectors ($\dot{I}_{1+} - \dot{I}_{6+}$) and three zero current vectors ($\dot{I}_7 - \dot{I}_9$).

As the MC's output is connected to the resonant tank, the output current direction of the MC will change in each switching period. As a result, six extra active vectors ($\dot{I}_{1-} - \dot{I}_{6-}$) have to be used. When the primary-side current i_1 is larger than 0, the positive current vectors $\dot{I}_{1+}$ to $\dot{I}_{6+}$ will be used. Conversely, when the primary-side current i_1 is smaller than 0, the negative current vectors $\dot{I}_{1-}$ to $\dot{I}_{6-}$ will be used.

In each sector, the current reference vector $\dot{I}_g$ is synthesized by two adjacent active vectors and one zero vector in a single switching period. For instance, in sector I, positive vectors $\dot{I}_{1+}$ and $\dot{I}_{2+}$ or negative vectors $\dot{I}_{1-}$ and $\dot{I}_{2-}$ will be used. Also, to minimize switching times, the zero vector $\dot{I}_7$ will be chosen for sector I.

Comparing the waveforms in Fig. 4, it is seen that I_o is a dc current while i_1 is an ac current. First, the phase angle of i_1 will have effects on the synthesized vector $\dot{I}_g$. Second, as the dwell time calculation for the current source converter is based on I_o, the expressions of conventional dwell time will not be applicable to the MC system. The elimination of the above-mentioned effects will be discussed in the following parts.

B. Reactive Component Cancellation

For conventional modulation methods [18], [19], [20], as shown in Fig. 7(a), the modulation waveform displays a half-wave symmetric pattern, which is characterized by a shift of one-half period and inversion. An inherent challenge of this approach lies in the sensitivity of the synthesized vectors' accuracy to the phase shift $\theta_P = \omega_s T_P$ (defined in Fig. 3) between voltage v_1 and current i_1. In practice, due to the load variation and component tolerance, a phase shift will inevitably occur between v_1 and i_1, which will result in a severe distortion in the low-frequency ac waveforms on either the grid side or load side, thereby raising the THD value.

The phase-shift effect on THD can be explained by considering the reactive components generated in the resonant tank, and a simple analysis is given in the following. As shown in Fig. 3 or Fig. 7, v_{1_1} is the fundamental component of v_1 and corresponds to the fundamental vector $\dot{V}_1$ in Section II. In addition, i_{1_act} and i_{1_rct} denote the active and reactive components of i_1, respectively. With the above-mentioned definitions, the time domain expressions of v_{1_1}, i_1, i_{1_act}, and i_{1_rct} can be obtained as

$$\begin{cases} v_{1\_1} = V_1 \sin(\omega_s t) \\ i_1 = I_1 \sin(\omega_s t - \omega_s T_P) \\ i_{1\_act} = I_1 \cos(\omega_s T_P) \sin(\omega_s t) \\ i_{1\_rct} = I_1 \sin(\omega_s T_P) \sin\left(\omega_s t - \dfrac{\pi}{2}\right). \end{cases} \tag{10}$$

If there is no phase shift (i.e., $T_P = 0$), we can have $i_{1\_act} = I_1 \sin(\omega_s t)$ and $i_{1\_rct} = 0$. In this case, i_1 consists entirely of i_{1_act}. If the phase shift exists (i.e., $T_P \neq 0$), i_1 will be composed of both i_{1_act} and i_{1_rct}. When synthesizing the grid current, we hope to have only i_{1_act} to avoid distortion caused by i_{1_rct} [21]. Thus, we will check the reactive component in different modulation waveforms.

For the half-wave symmetric modulation, as shown in Fig. 7(a), the integration of v_1 and i_{1_rct} during the intervals ($d_1 T_s$, $d_2 T_s$) and ($d_4 T_s$, $d_5 T_s$) can be calculated as

$$\begin{cases} Q_{12} = \dfrac{V_{uw} I_1 \sin(\omega_s T_P)}{\omega_s} \left[\sin(d_1 \omega_s T_s) - \sin(d_2 \omega_s T_s)\right] \\ Q_{45} = \dfrac{V_{uw} I_1 \sin(\omega_s T_P)}{\omega_s} \left[\sin(d_5 \omega_s T_s) - \sin(d_4 \omega_s T_s)\right]. \end{cases} \tag{11}$$

Considering $d_4 = d_1 + 1/2$ and $d_5 = d_2 + 1/2$, we can conclude that $Q_{12} = Q_{45}$ from (11). It is seen that the reactive component cannot be canceled out for the half-wave symmetric modulation.

For the periodic flip modulation, as shown in Fig. 7(b), the half-wave symmetric modulation is executed in the first switching period. Following this, a flipped waveform is implemented in the next switching period. Through this method, we can obtain

$$\begin{cases} Q_{12} = \dfrac{V_{uw} I_1 \sin(\omega_s T_P)}{\omega_s} \left[\sin(d_1 \omega_s T_s) - \sin(d_2 \omega_s T_s)\right] \\ Q_{67} = \dfrac{V_{uw} I_1 \sin(\omega_s T_P)}{\omega_s} \left[\sin(d_6 \omega_s T_s) - \sin(d_7 \omega_s T_s)\right]. \end{cases} \tag{12}$$

With the relationships of $d_6 = 3/2 - d_2$ and $d_7 = 3/2 - d_1$, it can be concluded that $Q_{12} + Q_{67} = 0$, indicating the cancellation of reactive components for the periodic flip modulation.

Indeed, it is feasible to cancel out the reactive component in a single switching period. As shown in Fig. 3, in the first half switching period, the waveform is kept the same as the half-wave symmetric modulation. In the latter half, the half-wave symmetric waveform is flipped, creating an antisymmetric waveform characterized by rotational symmetry with respect to the origin. By applying a similar integration method, we can

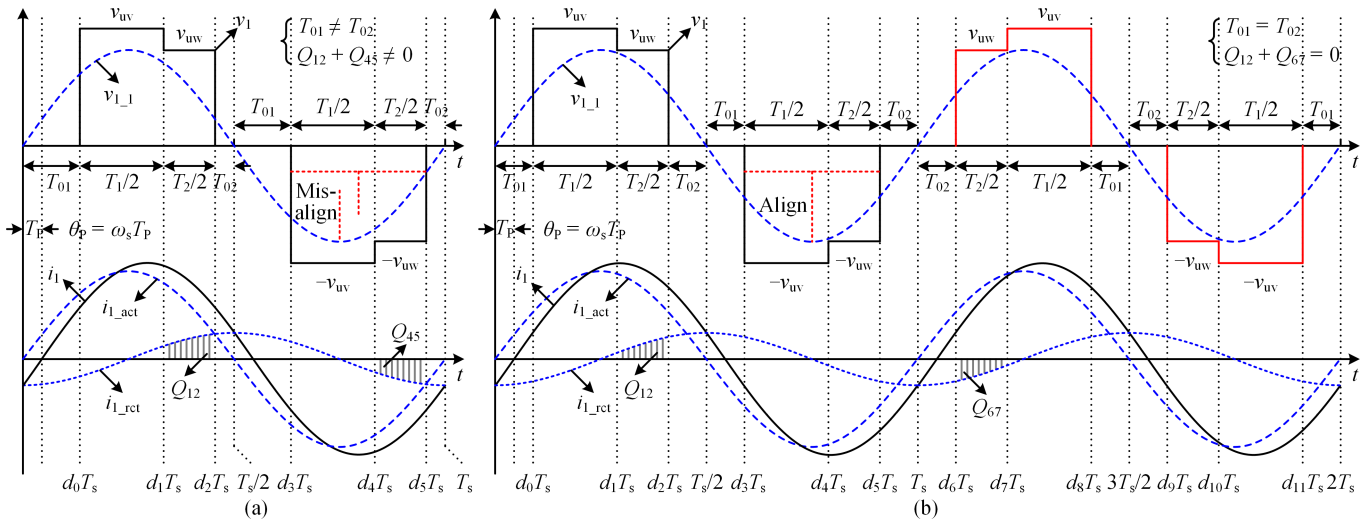

Fig. 7. Modulation waveforms of MCs in sector I. (a) Half-wave symmetric waveform. (b) Periodic flip waveform.

have

$$\begin{cases} Q_{12} = \dfrac{V_{uw} I_1 \sin(\omega_s T_P)}{\omega_s} \left[\sin(d_1 \omega_s T_s) - \sin(d_2 \omega_s T_s)\right] \\ Q_{34} = \dfrac{V_{uw} I_1 \sin(\omega_s T_P)}{\omega_s} \left[\sin(d_4 \omega_s T_s) - \sin(d_3 \omega_s T_s)\right]. \end{cases} \tag{13}$$

Similarly, with the relationships of $d_3 = 1 - d_2$ and $d_4 = 1 - d_1$, it can be observed that $Q_{12} + Q_{34} = 0$. Therefore, reactive components can also be canceled out for the antisymmetric modulation, and thus the effect of the phase shift can be mitigated. While the antisymmetric waveform has been used in a previous study [22], the advantage of reactive component elimination has not been revealed so far.

C. Dwell Time Calculation

Another challenge in implementing the modulation strategy is to determine the dwell time. For a detailed exploration of the dwell time, we first examine the fundamental components of various modulation waveforms.

The Fourier series and fundamental components of the above-mentioned three modulation waveforms are summarized in Table I, where $D_1 = T_1/T_s$ and $D_2 = T_2/T_s$. From the table, it can be observed that the fundamental harmonic expressions v_{1_1} are identical for the periodic flip waveform and the antisymmetric waveform. However, the half-wave symmetric waveform includes an extra cosine item in its fundamental harmonic expression. The additional item will make the central axes of v_1 and v_{1_1} not align for the half-wave symmetric waveform, as shown in Fig. 7(a). In contrast, the central axes of v_1 can align with those of v_{1_1} for the periodic flip waveform and the antisymmetric waveform, as shown in Figs. 7(b) and 3. More specifically, it can be deduced that $T_{01} \neq T_{02}$ is for the half-wave symmetric waveform, while $T_{01} = T_{02}$ is for both the periodic flip waveform and the antisymmetric waveform.

In previous studies using half-wave symmetric waveforms, it has been typically assumed that either $T_{01} = T_{02}$ for dwell time calculation [19] or current i_1 is a dc component to directly apply the dwell time expression of the current source converter to the MC-based system [18], [20]. However, these solutions often result in poor THD performance. It has been mentioned in a previous work [21] that an analytical solution is unavailable, prompting the use of numerical solvers to determine the dwell time. Also, in the study involving antisymmetric waveforms [22], the zero vector time of the current source converter has been used for resonant current scenarios.

Indeed, an analytical solution of dwell time can be found for the periodic flip or antisymmetric waveforms by leveraging the condition $T_{01} = T_{02}$. Next, we will determine the dwell time and use the antisymmetric waveform as a case study. Referring to Fig. 3, the grid current in sector I in one switching period can be expressed as

$$\begin{cases} i_u = |i_1|, \ t \in (d_0T_s, d_2T_s) \bigcup (d_3T_s, d_5T_s) \\ i_v = -|i_1|, \ t \in (d_0T_s, d_1T_s) \bigcup (d_4T_s, d_5T_s) \\ i_w = -|i_1|, \ t \in (d_1T_s, d_2T_s) \bigcup (d_3T_s, d_4T_s). \end{cases} \tag{14}$$

Since the reactive component can be canceled out, only the active component of i_1 is considered in (14). Then, the mean values of i_u, i_v, and i_w over one switching period can be expressed as

$$\begin{cases} \bar{i}_u = \dfrac{2}{T_s} \displaystyle\int_{d_0T_s}^{d_2T_s} I_1 \sin(\omega_s t)\, dt \\ \bar{i}_v = -\dfrac{2}{T_s} \displaystyle\int_{d_0T_s}^{d_1T_s} I_1 \sin(\omega_s t)\, dt \\ \bar{i}_w = -\dfrac{2}{T_s} \displaystyle\int_{d_1T_s}^{d_2T_s} I_1 \sin(\omega_s t)\, dt. \end{cases} \tag{15}$$

Meanwhile, to maintain a sinusoidal waveform of the grid-side current, the average of i_u, i_v, and i_w also needs to meet

$$\begin{cases} \bar{i}_u = I_g \cos(\theta_g) \\ \bar{i}_v = I_g \cos(\theta_g - 2\pi/3) \\ \bar{i}_w = I_g \cos(\theta_g + 2\pi/3) \end{cases} \tag{16}$$

TABLE I
FOURIER SERIES OF VARIOUS MODULATION WAVEFORMS

Waveform	Expression
	$v_{\mathrm{l}}(t)=\begin{cases} v_{\mathrm{uv}},\ t\in(d_0T_{\mathrm{s}},d_1T_{\mathrm{s}})\,;\ v_{\mathrm{uw}},\ t\in(d_1T_{\mathrm{s}},d_2T_{\mathrm{s}}) \\ -v_{\mathrm{uv}},\ t\in(d_3T_{\mathrm{s}},d_4T_{\mathrm{s}})\,;\ -v_{\mathrm{uw}},\ t\in(d_4T_{\mathrm{s}},d_5T_{\mathrm{s}}) \\ 0,\ \text{others} \end{cases}$
Half-wave symmetric	$v_{\mathrm{l}}(t)=\frac{4}{\pi}\sum_{k=1}^{\infty}\frac{1}{k}\sin\frac{k\pi}{2}\left[\begin{array}{l}\sin\frac{kD_1\pi}{2}\sin\frac{kD_2\pi}{2}(v_{\mathrm{uv}}-v_{\mathrm{uw}})\cos(k\omega_{\mathrm{s}}t)+\\ \left(v_{\mathrm{uv}}\sin\frac{kD_1\pi}{2}\cos\frac{kD_2\pi}{2}+v_{\mathrm{uw}}\sin\frac{kD_2\pi}{2}\cos\frac{kD_1\pi}{2}\right)\sin(k\omega_{\mathrm{s}}t)\end{array}\right]$
	$v_{\mathrm{l}\sqcup}(t)=\frac{4}{\pi}\left[\begin{array}{l}\sin\frac{D_1\pi}{2}\sin\frac{D_2\pi}{2}(v_{\mathrm{uv}}-v_{\mathrm{uw}})\cos(\omega_{\mathrm{s}}t)+\\ \left(v_{\mathrm{uv}}\sin\frac{D_1\pi}{2}\cos\frac{D_2\pi}{2}+v_{\mathrm{uw}}\sin\frac{D_2\pi}{2}\cos\frac{D_1\pi}{2}\right)\sin(\omega_{\mathrm{s}}t)\end{array}\right]$
	$v_{\mathrm{l}}(t)=\begin{cases} v_{\mathrm{uv}},\ t\in(d_0T_{\mathrm{s}},d_1T_{\mathrm{s}})\bigcup(d_7T_{\mathrm{s}},d_8T_{\mathrm{s}})\,;\ v_{\mathrm{uw}},\ t\in(d_1T_{\mathrm{s}},d_2T_{\mathrm{s}})\bigcup(d_6T_{\mathrm{s}},d_7T_{\mathrm{s}}) \\ -v_{\mathrm{uv}},\ t\in(d_3T_{\mathrm{s}},d_4T_{\mathrm{s}})\bigcup(d_{10}T_{\mathrm{s}},d_{11}T_{\mathrm{s}})\,;\ -v_{\mathrm{uw}},\ t\in(d_4T_{\mathrm{s}},d_5T_{\mathrm{s}})\bigcup(d_9T_{\mathrm{s}},d_{10}T_{\mathrm{s}}) \\ 0,\ \text{others} \end{cases}$
Periodic flip	$v_{\mathrm{l}}(t)=-\frac{8}{\pi}\sum_{k=1}^{\infty}\frac{\cos(k\pi)}{k}\sin\frac{k\pi}{4}\left[\begin{array}{l}v_{\mathrm{uv}}\sin\frac{kD_1\pi}{4}\cos\frac{k(2+D_2)\pi}{4}+\\ v_{\mathrm{uw}}\sin\frac{kD_2\pi}{4}\cos\frac{k(-2+D_1)\pi}{4}\end{array}\right]\sin\left(k\frac{\omega_{\mathrm{s}}}{2}t\right)$
	$v_{\mathrm{l}\sqcup}(t)=\frac{4}{\pi}\left(v_{\mathrm{uv}}\sin\frac{D_1\pi}{2}\cos\frac{D_2\pi}{2}+v_{\mathrm{uw}}\sin\frac{D_2\pi}{2}\cos\frac{D_1\pi}{2}\right)\sin(\omega_{\mathrm{s}}t)$
	$v_{\mathrm{l}}(t)=\begin{cases} v_{\mathrm{uv}},\ t\in(d_0T_{\mathrm{s}},d_1T_{\mathrm{s}})\,;\ v_{\mathrm{uw}},\ t\in(d_1T_{\mathrm{s}},d_2T_{\mathrm{s}}) \\ -v_{\mathrm{uw}},\ t\in(d_3T_{\mathrm{s}},d_4T_{\mathrm{s}})\,;\ -v_{\mathrm{uv}},\ t\in(d_4T_{\mathrm{s}},d_5T_{\mathrm{s}}) \\ 0,\ \text{others} \end{cases}$
Antisymmetric	$v_{\mathrm{l}}(t)=-\frac{4}{\pi}\sum_{k=1}^{\infty}\frac{\cos(k\pi)}{k}\left[\begin{array}{l}v_{\mathrm{uv}}\sin\frac{kD_1\pi}{2}\sin\frac{k(1+D_2)\pi}{2}+\\ v_{\mathrm{uw}}\sin\frac{kD_2\pi}{2}\sin\frac{k(1-D_1)\pi}{2}\end{array}\right]\sin(k\omega_{\mathrm{s}}t)$
	$v_{\mathrm{l}\sqcup}(t)=\frac{4}{\pi}\left(v_{\mathrm{uv}}\sin\frac{D_1\pi}{2}\cos\frac{D_2\pi}{2}+v_{\mathrm{uw}}\sin\frac{D_2\pi}{2}\cos\frac{D_1\pi}{2}\right)\sin(\omega_{\mathrm{s}}t)$

where I_{g} and θ_{g} are the amplitude and phase angle of the grid-side current, respectively. Combining (15) and (16), we get

$$\begin{cases}\cos(\omega_{\mathrm{s}}d_0T_{\mathrm{s}})-\cos(\omega_{\mathrm{s}}d_2T_{\mathrm{s}})=2\,\mathrm{m}\cos(\theta_{\mathrm{g}}) \\ \cos(\omega_{\mathrm{s}}d_1T_{\mathrm{s}})-\cos(\omega_{\mathrm{s}}d_0T_{\mathrm{s}})=2\,\mathrm{m}\cos(\theta_{\mathrm{g}}-2\pi/3\,) \\ \cos(\omega_{\mathrm{s}}d_2T_{\mathrm{s}})-\cos(\omega_{\mathrm{s}}d_1T_{\mathrm{s}})=2\,\mathrm{m}\cos(\theta_{\mathrm{g}}+2\pi/3\,)\end{cases}\tag{17}$$

where $m=\pi I_{\mathrm{g}}/(2\sqrt{2}I_1)$ is the modulation index of the MC. Considering the constraint of $i_{\mathrm{u}}+i_{\mathrm{v}}+i_{\mathrm{w}}=0$, only two equations are effective in (17). However, there are three variables d_0, d_1, and d_2 to be solved, so an extra equation is required. With $T_{01}=T_{02}$, we find that $d_0+d_2=1/2$. Then, the solution of (17) can be obtained as

$$\begin{cases}d_0=\dfrac{\arccos[m\cos(\theta_{\mathrm{g}})]}{2\pi} \\ d_1=\dfrac{\arccos[m\cos(\theta_{\mathrm{g}})+2\mathrm{m}\cos(\theta_{\mathrm{g}}-2\pi/3\,)]}{2\pi} \\ d_2=\dfrac{\pi-\arccos[m\cos(\theta_{\mathrm{g}})]}{2\pi}.\end{cases}\tag{18}$$

Similarly, the dwell time expressions in other sectors can be obtained, and the results are summarized in Table II . By unifying the expressions for d_0, d_1, and d_2, we obtain

$$\begin{cases}d_0=(\arccos T_{\mathrm{A}})/2\pi \\ d_1=[\arccos(T_{\mathrm{A}}+2T_{\mathrm{B}})]/2\pi \\ d_2=(\pi-\arccos T_{\mathrm{A}})/2\pi\end{cases}\tag{19}$$

where

$$\begin{cases}T_{\mathrm{A}}=m\cos\left[\theta_{\mathrm{g}}-\dfrac{\pi}{3}(N-1)\right] \\ T_{\mathrm{B}}=m\cos\left[\theta_{\mathrm{g}}-\dfrac{\pi}{3}(N+1)\right]\end{cases}\tag{20}$$

and N is the sector location.

D. Implementation

The implementation of the proposed modulation strategy is shown in Fig. 8. First, the grid-side voltages (v_{u}, v_{v}, v_{w}) are sampled. Through the Clarke transformation and Park transformation, we can obtain the dq components (v_{d}, v_{q}) of the grid voltages. After the phase-locked loop control, the phase angle (θ_{g}) of the grid input can be obtained. Combining the grid phase angle and the modulation index (m), the reference signals

TABLE II
SUMMARY OF DWELL TIME EXPRESSIONS

Sector	d_0	d_1	d_2
I	$\frac{\arccos[m\cos(\theta_g)]}{2\pi}$	$\frac{\arccos[m\cos(\theta_g)+2m\cos(\theta_g-2\pi/3)]}{2\pi}$	$\frac{\pi-\arccos[m\cos(\theta_g)]}{2\pi}$
II	$\frac{\pi-\arccos[m\cos(\theta_g+2\pi/3)]}{2\pi}$	$\frac{\pi-\arccos[m\cos(\theta_g+2\pi/3)+2m\cos(\theta_g)]}{2\pi}$	$\frac{\arccos[m\cos(\theta_g+2\pi/3)]}{2\pi}$
III	$\frac{\arccos[m\cos(\theta_g-2\pi/3)]}{2\pi}$	$\frac{\arccos[m\cos(\theta_g-2\pi/3)+2m\cos(\theta_g+2\pi/3)]}{2\pi}$	$\frac{\pi-\arccos[m\cos(\theta_g-2\pi/3)]}{2\pi}$
IV	$\frac{\pi-\arccos[m\cos(\theta_g)]}{2\pi}$	$\frac{\pi-\arccos[m\cos(\theta_g)+2m\cos(\theta_g-2\pi/3)]}{2\pi}$	$\frac{\arccos[m\cos(\theta_g)]}{2\pi}$
V	$\frac{\arccos[m\cos(\theta_g+2\pi/3)]}{2\pi}$	$\frac{\arccos[m\cos(\theta_g+2\pi/3)+2m\cos(\theta_g)]}{2\pi}$	$\frac{\pi-\arccos[m\cos(\theta_g+2\pi/3)]}{2\pi}$
VI	$\frac{\pi-\arccos[m\cos(\theta_g-2\pi/3)]}{2\pi}$	$\frac{\pi-\arccos[m\cos(\theta_g-2\pi/3)+2m\cos(\theta_g+2\pi/3)]}{2\pi}$	$\frac{\arccos[m\cos(\theta_g-2\pi/3)]}{2\pi}$

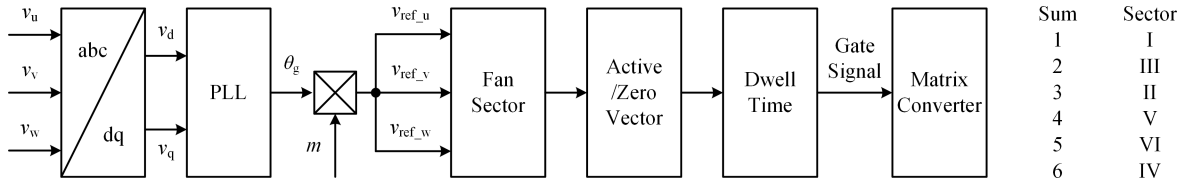

Fig. 8. Implementation of the proposed modulation strategy.

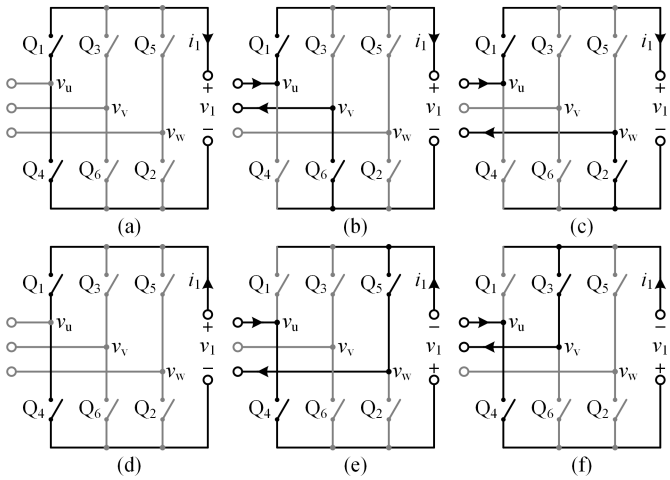

Fig. 9. Circuit modes of the MC corresponding to waveforms in Fig. 3 with $\theta_P = 0$. (a) (0, d_0T_s) or (d_2T_s, $T_s/2$). (b) (d_0T_s, d_1T_s). (c) (d_1T_s, d_2T_s). (d) ($T_s/2$, d_3T_s) or (d_5T_s, T_s). (e) (d_3T_s, d_4T_s). (f) (d_4T_s, d_5T_s).

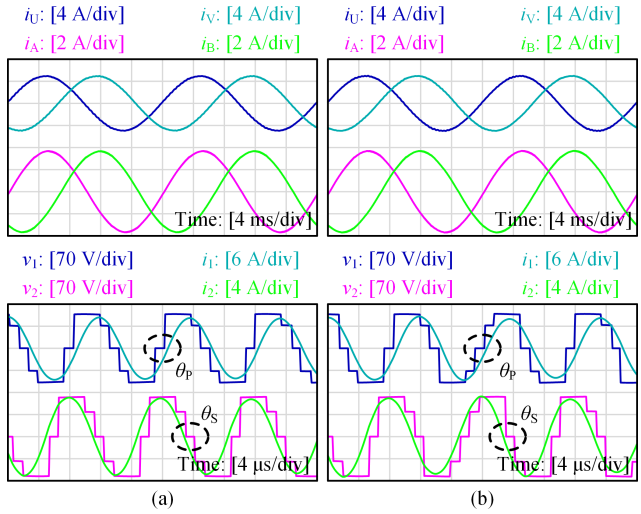

Fig. 10. Simulation waveforms. (a) Antisymmetric waveforms with $\theta'_{PS} = 30°$ and $R_L = 20\,\Omega$. (b) Periodic flip waveforms with $\theta'_{PS} = 30°$ and $R_L = 20\,\Omega$.

$(v_{ref\_u},\ v_{ref\_v}, v_{ref\_w})$ are obtained

$$\begin{cases} v_{ref\_u} = m\cos(\theta_g) \\ v_{ref\_v} = m\cos\left(\theta_g - \frac{2\pi}{3}\right) \\ v_{ref\_w} = m\cos\left(\theta_g + \frac{2\pi}{3}\right). \end{cases} \tag{21}$$

The sector location can be determined based on the sign of the input voltage, i.e.,

$$\text{Sum} = \text{sign}(v_{ref\_u}) + 2\,\text{sign}(v_{ref\_v}) + 4\,\text{sign}(v_{ref\_w}) \tag{22}$$

where

$$\text{sign}(v_{ref\_i}) = \begin{cases} 1 & v_{ref\_i} > 0 \\ 0 & v_{ref\_i} \le 0 \end{cases} \quad i \in \{u, v, w\}. \tag{23}$$

The mapping relationship between the sum values and sectors is shown in Fig. 8. According to the fan sector location, the selection of active and zero vectors can be determined from Fig. 6. Meanwhile, the dwell time of the selected vectors is calculated using (19). With the obtained fan sector and the dwell time, the gate signals can finally be generated for the MC through the enhanced pulse-width modulator of the controller.

E. Circuit Modes

Based on the proposed modulation method, the circuit modes of the MC are analyzed in this part. Taking the antisymmetric

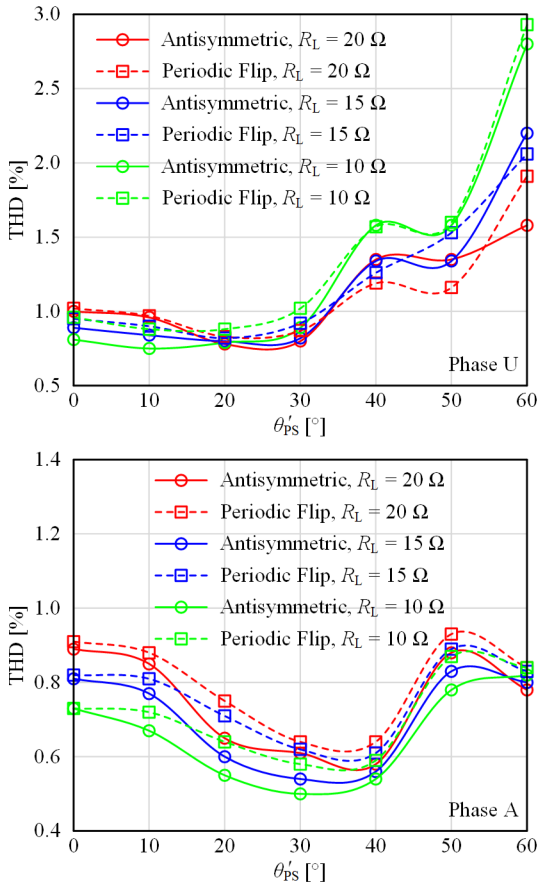

Fig. 11. Simulation results of THD values for antisymmetric waveforms and periodic flip waveforms.

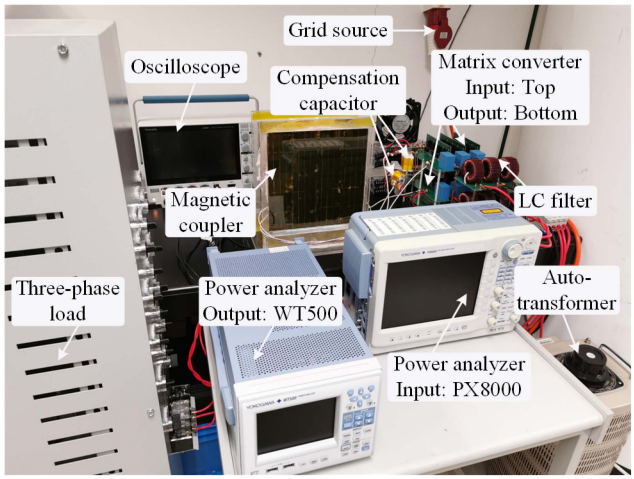

Fig. 12. Experimental prototype of dual MC-based WPT system.

modulation waveform (see Fig. 3) as an example, the corresponding circuit modes under zero input phase angle conditions are plotted in Fig. 9.

1) $(0, d_0T_s)$ or $(d_2T_s, T_s/2)$: As shown in Fig. 9(a), current i_1 flows through Q_1 and Q_4 in freewheeling modes and in positive directions. In this case, the switching devices conduct in one bridge arm and the MC operates with the zero vector $\dot{I}_7$.
2) (d_0T_s, d_1T_s): As shown in Fig. 9(b), current i_1 flows through Q_1 and Q_6 in positive directions. The grid source supplies power to the resonant tank, and the input voltage of the resonant tank equals v_{uv}. For this scenario, the MC operates with the active vector $\dot{I}_{1+}$.
3) (d_1T_s, d_2T_s): As shown in Fig. 9(c), current i_1 flows positively through Q_1 and Q_2. The power supply voltage changes from v_{uv} to v_{uw}, and the MC operates with the active vector $\dot{I}_{2+}$.
4) $(T_s/2, d_3T_s)$ or (d_5T_s, T_s): As shown Fig. 9(d), current i_1 flows through Q_1 and Q_4 in freewheeling modes while in negative directions. The MC also operates with the zero vector $\dot{I}_7$.
5) (d_3T_s, d_4T_s): As shown in Fig. 9(e), current i_1 flows in negative directions through Q_4 and Q_5. Meanwhile, the power supply voltage is reversed and becomes $-v_{uw}$. The MC operates with the active vector $\dot{I}_{2-}$.
6) (d_4T_s, d_5T_s): As shown in Fig. 9(f), current i_1 flows negatively through Q_3 and Q_4. The power supply voltage becomes $-v_{uv}$, and the MC operates with the active vector $\dot{I}_{1-}$.

IV. Simulation and Experimental Verification

In this section, simulation results are first provided to showcase the comparable performance of periodic flip modulation and antisymmetric modulation. Subsequently, experimental results are presented to demonstrate the operation of the proposed dual MC system and the effectiveness of the proposed modulation strategy. Finally, a comparison with existing research and potential research challenges are presented.

For both simulation and experimental results, the current THD is calculated by the ratio of the rms amplitude of all higher harmonics to the rms amplitude of the fundamental frequency (f_g). Besides, considering the power quality standard requirements [30], [31] and the power analyzer equipment limitations [32], the maximum harmonic order is set to 50.

A. Simulation Results

The dual MC-based WPT system is built in Simulink with parameters listed in Table III. Simulation waveforms of the antisymmetric modulation and the periodic flip modulation are shown in Fig. 10, displaying similar results of i_U, i_V, i_A, and i_B for both modulation strategies. In addition, with the derived dwell time, both modulation methods can have a small distortion in the grid-side and load-side currents despite a significant phase shift of θ_P and θ_S.

Moreover, THD values of grid-side and load-side currents are simulated across various loads R_L and phase-shift angles θ'_{PS}, as shown in Fig. 11. These curves demonstrate that both antisymmetric and periodic flip modulation can maintain the THD levels below 5% under a wide load range [30], [31]. Moreover, the THD results of these two modulation

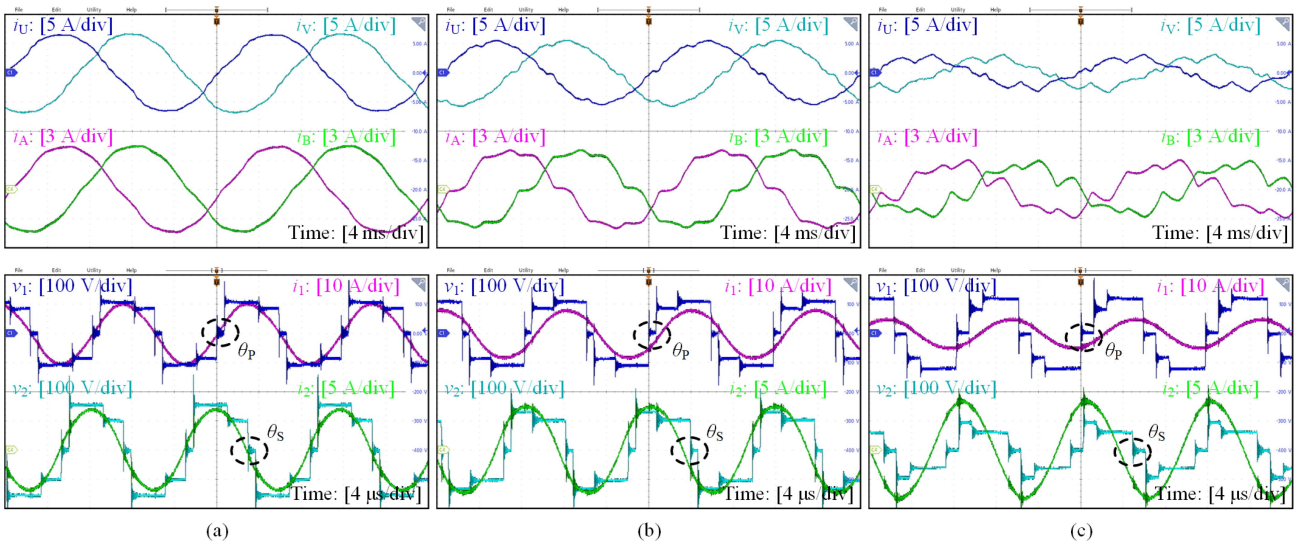

Fig. 13. Measured waveforms of half-wave symmetric modulation with $R_L = 20\,\Omega$. (a) $\theta'_{PS} = 0°$. (b) $\theta'_{PS} = 30°$. (c) $\theta'_{PS} = 60°$.

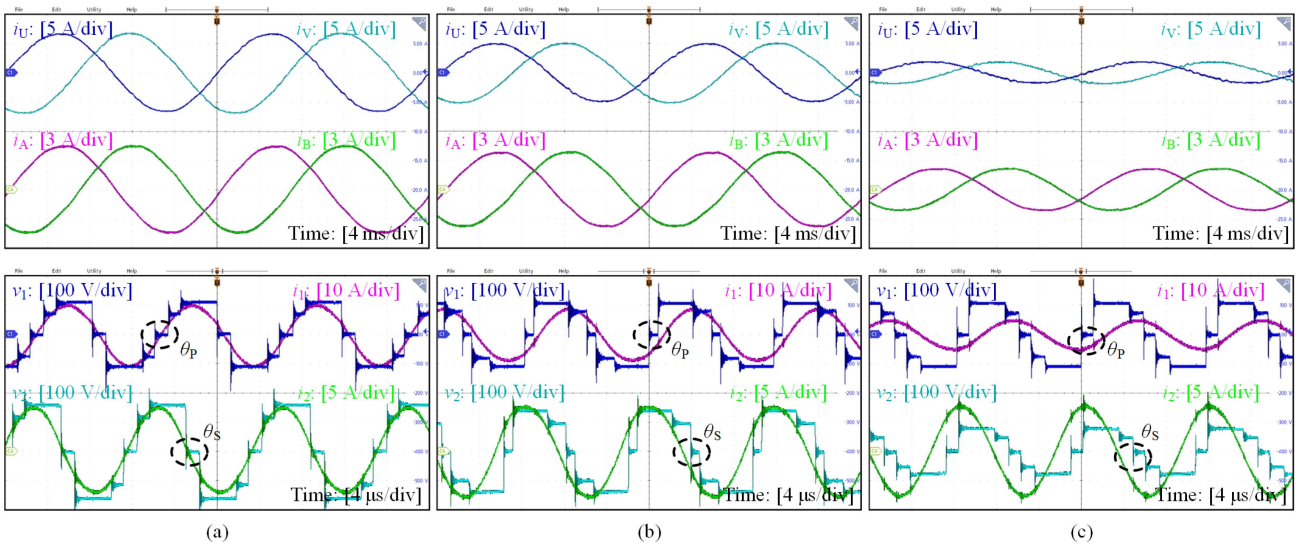

Fig. 14. Measured waveforms of antisymmetric modulation with $R_L = 20\,\Omega$. (a) $\theta'_{PS} = 0°$. (b) $\theta'_{PS} = 30°$. (c) $\theta'_{PS} = 60°$.

waveforms exhibit minimal variance. The simulation waveforms and THD results indicate that the antisymmetric modulation and periodic flip modulation can achieve an equivalent performance for the dual matrix system. For convenience, we only implement the antisymmetric modulation in the experiment.

B. Experimental Platform

A prototype of the dual MC-based WPT system is also fabricated to verify the theoretical analysis, as shown in Fig. 12. The experimental parameters are the same as the simulation model and are given in Table III.

In the experiment, power is drawn from the three-phase grid source through an autotransformer. Both grid-side and load-side MCs are composed of 12 SiC MOSFETs C3M0025065 K, and DSP28377D is used as the controller. The magnetic coupler incorporates the Litz wires (400 × 0.1 mm) and the magnetic cores PLT64/50/5. Three-phase inductor–resistor series branches are used as the load. Moreover, Tektronix MDO34 is used to display voltage and current waveforms. Power analyzers PX8000 and WT500 are used to measure the input and output THD values, respectively.

C. Experimental Results

First, the half-wave symmetric modulation is applied to the system with experimental waveforms shown in Fig. 13. At $\theta'_{PS} = 0°$, where θ_P and θ_S have minimal deviation, both the grid-side and load-side currents exhibit low distortion. However, as θ'_{PS} increases to 30° or 60°, implicated by the changes of θ_P and θ_S in Fig. 13, distortion intensifies in both grid-side and load-side currents.

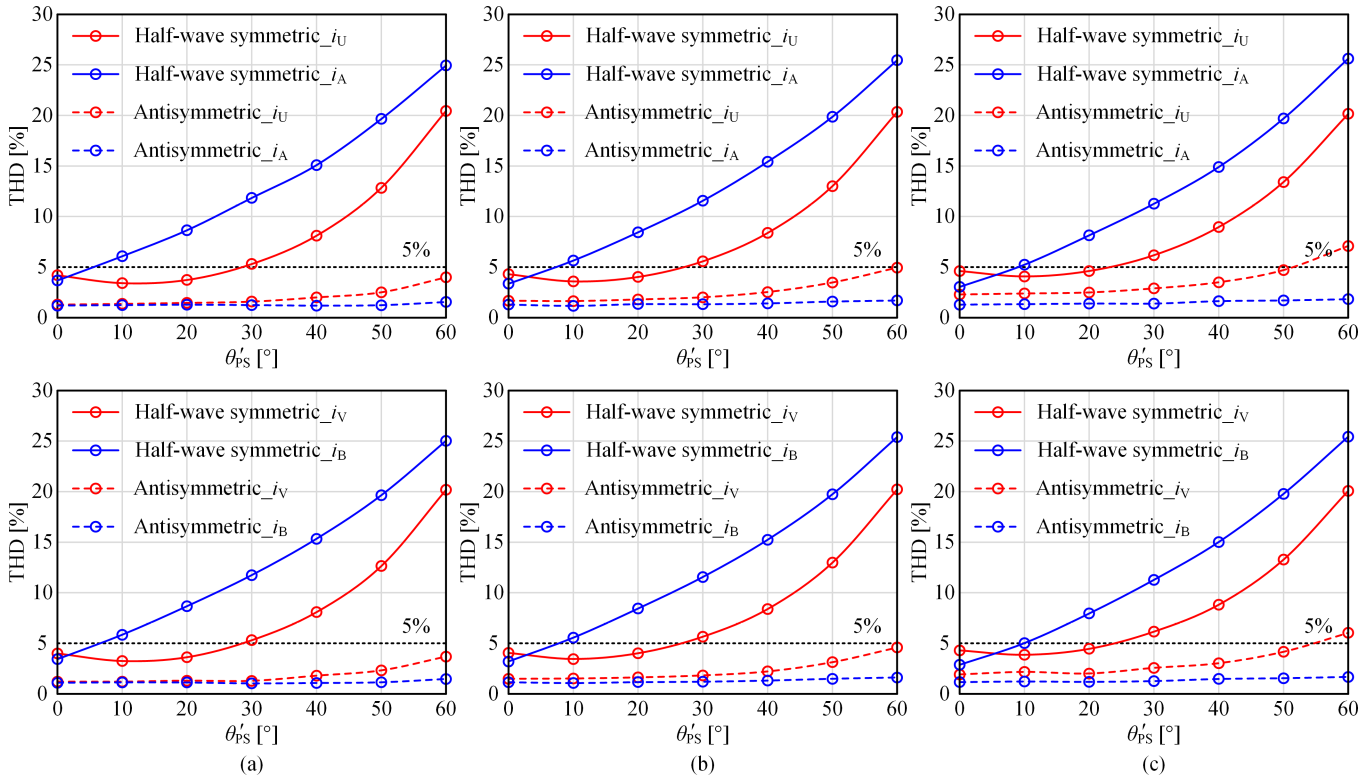

Fig. 15. Measured THD curves. (a) $R_L = 20\,\Omega$. (b) $R_L = 15\,\Omega$. (c) $R_L = 10\,\Omega$.

TABLE III
SIMULATION AND EXPERIMENT PARAMETERS

	Parameter	Type/value
Specification	Grid line voltage (V_g)	3×110 V
	Grid frequency (f_g)	50 Hz
	Grid filter (L_f, C_f)	500 μH, 10 μF
	Load filter (C'_f)	10 μF
	Load inductance (L'_f)	500 μH
	Load resistance (R_f)	10/15/20 Ω
MC	MOSFETs-Pri. (Q_1–Q_6)	C3M0025065K
	MOSFETs-Sec. (S_1–S_6)	C3M0025065K
	Switching frequency (f_s)	85 kHz
	Controller	TMS320F28377D
Magnetic coupler	Self inductance-Pri. (L_P)	117.2 μH
	Self inductance-Sec. (L_S)	117.1 μH
	Mutual inductance (M)	30.95 μH
	Coil turns (n_P, n_S)	17, 17
	Coil size (d_{coil})	254 mm
	Transfer distance (d_{gap})	100 mm
Resonant capacitor	Theory-Pri. (C_P)	29.91 nF
	Theory-Sec. (C_S)	29.94 nF
	Measure-Pri. (C_P)	30.11 nF
	Measure-Sec. (C_S)	30.12 nF

Next, the system is operated with antisymmetric modulation, and the corresponding waveforms are provided in Fig. 14. With $\theta'_{PS} = 0°$, where θ_P and θ_S have little shifts, the antisymmetric modulation can also achieve a good THD performance, as shown in Fig. 14(a). Besides, comparing Figs. 13(a) and 14(a), it is observed that the antisymmetric modulation has less distortion in either the grid-side or load-side current. This is because of $T_{01} \neq T_{02}$ (refer to Fig. 7 for definition) for the half-wave symmetric waveform. Making an approximation of $T_{01} = T_{02}$ for the half-wave symmetric waveform will lead to increased errors in dwell time calculations, thereby deteriorating the THD performance.

Moreover, as we change the phase angle of θ'_{PS} for power regulation, such as $\theta'_{PS} = 30°$ or $\theta'_{PS} = 60°$ in Fig. 14(b) and (c) respectively, it is seen that the amplitudes of the grid-side currents (i_U, i_V) and the load-side currents (i_A, i_B) decrease. Unlike the half-wave symmetric modulation, even in these cases, there is minimal distortion in grid-side and load-side currents when employing the antisymmetric modulation.

To further demonstrate the effectiveness of the proposed modulation method, the THD values of both grid-side and load-side currents are measured, as shown in Fig. 15. Regardless of the load values and phase-shift angles, the antisymmetric modulation can always outperform the half-wave symmetric modulation in terms of THD performance. In addition, it is seen that THD values significantly increase as θ'_{PS} increases for the half-wave symmetric modulation. In contrast, by employing the antisymmetric waveform and the derived dwell time, both grid-side and load-side THD values can always maintain below or around 5%, satisfying the IEEE standard requirements [30], [31].

Meanwhile, the harmonic distribution results are shown in Fig. 16. It also demonstrates that the proposed method (antisymmetric modulation) can significantly reduce the harmonic component than the conventional method (half-wave symmetric modulation). For example, as shown in Fig. 16(a), when $\theta'_{PS} = 0°$, the fifth harmonic accounts for 3.38% with the conventional

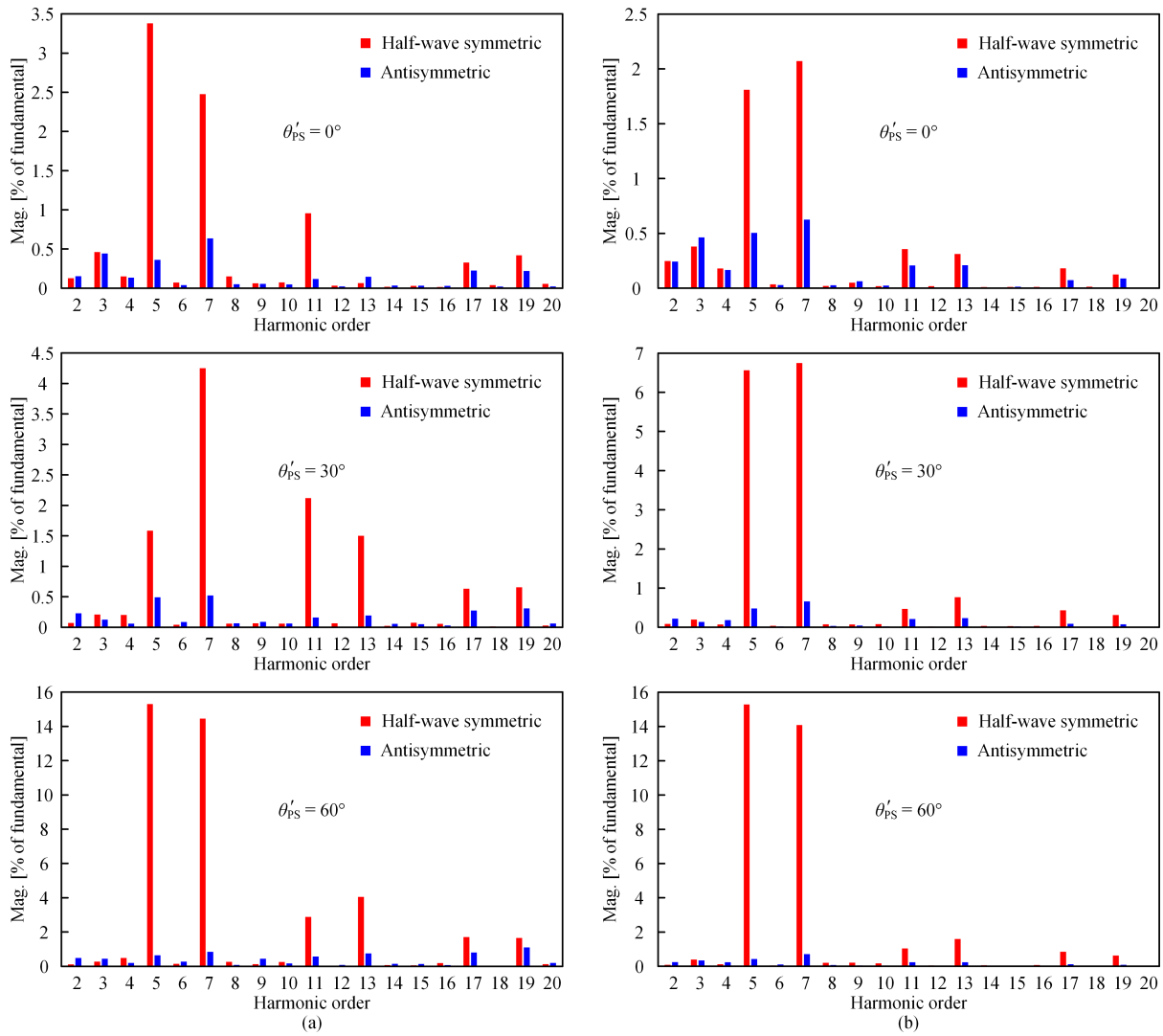

Fig. 16. Harmonic distribution with $R_L = 20\,\Omega$, measured up to the 50th harmonic and displayed up to the 20th harmonic. (a) Grid-side current i_U. (b) load-side current i_A.

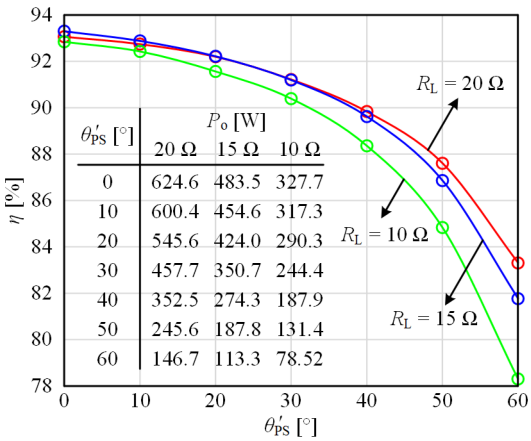

θ'_{PS} [°]	P_o [W] 20 Ω	15 Ω	10 Ω
0	624.6	483.5	327.7
10	600.4	454.6	317.3
20	545.6	424.0	290.3
30	457.7	350.7	244.4
40	352.5	274.3	187.9
50	245.6	187.8	131.4
60	146.7	113.3	78.52

Fig. 17. Measured system efficiency.

method, while it reduces to 0.363% with the proposed method. With the phase-shift angle increasing, such as $\theta'_{PS} = 60°$, the fifth harmonic will increase to 15.306% for the conventional method, while it only increases to 0.65% for the proposed method.

D. Comparison and Discussion

A comparison between existing work and this study is provided in Table IV. The conventional cascaded structure [4] only considers a dc power input. In practice, an additional ac–dc power conversion on the grid side is required since ac power is typically supplied. Meanwhile, an extra three-phase bridge inverter is needed to convert the WPT output to ac power for motor excitation. Also, electrolytic capacitors have to be used on both sides. On the other hand, the multicoil-based structure [9] realizes the load-side integration but is limited to motors with trapezoidal EMF. Besides, the grid side still has a multistage power conversion for this structure.

Previous studies on MC-based structures [11], [13], [17], [20], [21], [23] have primarily focused on battery loads, and the MC is normally employed on the grid side. Only two studies [12],

TABLE IV
COMPARISON OF PREVIOUS WORK AND THE PROPOSED METHOD

Ref.	Input Type	Input Structure	Output Type	Output Structure	Switching frequency	Coupling coefficient	Load type	THD	Maximum efficiency
[4]	Dc	Full-bridge inverter	3ph ac	Bridge inverter	85 kHz	0.20	Motor	N/A	88.80%
[9]	Dc	Full-bridge inverter	3×dc	Diode rectifier	85/100/115 kHz	0.22	Motor	N/A	83.58%
[11]	1ph ac	Half-bridge MC	Dc	Diode rectifier	30 kHz	N/A	Battery	N/A	N/A
[12]	Dc	Full-bridge inverter	1ph ac	Half-bridge MC	40 kHz	0.10	Motor	14.00%	N/A
[13]	1ph ac	Full-bridge MC	Dc	Active rectifier	20 kHz	0.29	Battery	4.80%	89.60%
[17]	3ph ac	Half-wave MC	Dc	Diode rectifier	50 kHz	0.20	Battery	N/A	85.00%
[18]	Dc	Full-bridge inverter	3ph ac	Bridge MC	85 kHz	0.57	Motor	N/A	N/A
[20]	3ph ac	Bridge MC	Dc	Diode rectifier	85 kHz	0.24	Battery	8.61%	90.00%
[21]	3ph ac	Bridge MC	Dc	Active bridge	85 kHz	0.41	Battery	3.27%	95.15%
[23]	3ph ac	Simplified bridge MC	Dc	Active rectifier	12 kHz	N/A	Battery	14.30%	88.20%
This work	3ph ac	Bridge MC	3ph ac	Bridge MC	85 kHz	0.26	Motor	1.11%	93.30%

[18] have explored the integration of MCs on the motor side. However, the grid side still adopts an ac–dc–ac configuration in these two studies. Our study here is a combination of the above-mentioned MC-based WPT systems, employing MCs on both grid and load sides, completely eliminating the electrolytic capacitors and further reducing the power conversion stages. Furthermore, the proposed modulation method in this study can achieve a notable enhancement in THD performance compared to previous studies. Importantly, the improved THD performance is achieved in a wide load range for this article, whereas earlier studies can only achieve desirable THD results for limited load conditions.

Nevertheless, there is still considerable work ahead for this research, particularly concerning the light-load efficiency. As shown in Fig. 17, a maximum efficiency of 93.3% has been achieved for the proposed system. It is worth noting that this efficiency encompasses the entire system from the grid ac input to the load ac output. However, this research can only realize the output control through the regulation of θ'_{PS}. The variation of θ'_{PS} will introduce lots of reactive power in the system. While the impact on THD can be mitigated, the reactive power will significantly affect the system's efficiency at light-load conditions. Therefore, an enhanced modulation strategy is still in demand for both THD and efficiency improvement.

Besides, the extensive use of power devices may increase the system cost of the proposed integrated structure compared to conventional cascaded systems. Fortunately, recent advancements in wide bandgap semiconductors, along with their increasing maturity, can help mitigate these cost concerns. In addition, the recent release of commercial bidirectional four-quadrant power devices enables more compact and efficient designs [33], [34]. The monolithic bidirectional switching devices will greatly simplify the MC-based system and accelerate its practical adoption.

V. CONCLUSION

This research aims to provide an integration solution for the WPT system with three-phase loads. Three-phase bridge MCs are adopted on both grid and load sides of the system to enable direct power transfer between the low-frequency ac and the high-frequency ac waveforms. For the proposed dual MC-based WPT system, the modulation strategy is investigated to improve the THD performance. By comparing different modulation waveforms, it is revealed that the reactive power effect of the resonant tank on THD can be diminished with the periodic flip waveform or the antisymmetric waveform. Besides, by utilizing the alignment property of the fundamental component in these waveforms, a precise and analytical solution of the modulation dwell time can be obtained, which could promote the feasibility of the proposed system. At last, a prototype is constructed to verify the theoretical analysis, achieving a minimum THD of approximately 1% for both grid-side and load-side currents, along with a peak efficiency of 93.3% from the grid side to the load side.

REFERENCES

[1] S. Y. R. Hui, Y. Yang, and C. Zhang, "Wireless power transfer: A paradigm shift for the next generation," *IEEE J. Emerg. Sel. Top. Power Electron.*, vol. 11, no. 3, pp. 2412–2427, Jun. 2023.
[2] V. B. Vu et al., "Operation of inductive charging systems under misalignment conditions: A review for electric vehicles," *IEEE Trans.Transp. Electrific.*, vol. 9, no. 1, pp. 1857–1887, Mar. 2023.
[3] J. Cai, B. Li, W. Hua, A. D. Cheok, Y. Yan, and X. Zhang, "Magnetic coupled wireless motor driving systems-an overview," *IEEE Trans. Power Electron.*, vol. 39, no. 6, pp. 7375–7391, Jun. 2024.
[4] M. Sato, G. Yamamoto, D. Gunji, T. Imura, and H. Fujimoto, "Development of wireless in-wheel motor using magnetic resonance coupling," *IEEE Trans. Power Electron.*, vol. 31, no. 7, pp. 5270–5278, Jul. 2016.
[5] Y. Chen, C. Gan, H. Shi, K. Ni, Z. Yang, and R. Qu, "Auxiliary circuit free maximum power efficiency tracking scheme for wireless motor system with source-load coupling," *IEEE Trans. Ind. Electron.*, vol. 70, no. 4, pp. 3414–3425, Apr. 2023.
[6] P. Jin, L. Chang, Y. Liu, Y. Guo, G. Lei, and J. Zhu, "Design and implementation of novel rotor side brushless controller with bidirectional wireless power transmission for doubly-fed machine," *IEEE Trans. Ind. Electron.*, vol. 71, no. 1, pp. 183–193, Jan. 2024.
[7] C. Jiang, K. T. Chau, C. Liu, and W. Han, "Design and analysis of wireless switched reluctance motor drives," *IEEE Trans. Ind. Electron.*, vol. 66, no. 1, pp. 245–254, Jan. 2019.
[8] H. Wang, K. T. Chau, C. H. T. Lee, and X. Tian, "Design and analysis of wireless resolver for wireless switched reluctance motors," *IEEE Trans. Ind. Electron.*, vol. 70, no. 3, pp. 2221–2230, Mar. 2023.
[9] K. Li, W. Ding, J. Yuan, and C. Du, "A decoupled multichannel based wireless SRM system with tunable compensation network and multifrequency pulse density control," *IEEE Trans. Ind. Electron.*, vol. 71, no. 2, pp. 1468–1480, Feb. 2024.

[10] L. Fang et al., "Design of wireless individual-drive system for variable-reluctance stepping motor," *IEEE Trans. Circuits Syst. II, Exp. Briefs*, vol. 69, no. 4, pp. 2141–2145, Apr. 2022.
[11] H. L. Li, A. P. Hu, and G. A. Covic, "A direct AC-AC converter for inductive power-transfer systems," *IEEE Trans. Power Electron.*, vol. 27, no. 2, pp. 661–668, Feb. 2012.
[12] A. Babaki, S. Vaez-Zadeh, A. Zakerian, and A. J. Natanzi, "Analysis and control of wireless motor drives with a single inverter in primary side," *IEEE Trans. Energy Convers.*, vol. 36, no. 2, pp. 930–939, Jun. 2021.
[13] S. Weerasinghe, U. K. Madawala, and D. J. Thrimawithana, "A matrix converter-based bidirectional contactless grid interface," *IEEE Trans. Power Electron.*, vol. 32, no. 3, pp. 1755–1766, Mar. 2017.
[14] S. Samanta and A. K. Rathore, "A new inductive power transfer topology using direct AC-AC converter with active source current waveshaping," *IEEE Trans. Power Electron.*, vol. 33, no. 7, pp. 5565–5577, Jul. 2018.
[15] M. Moghaddami and A. I. Sarwat, "Single-phase soft-switched AC-AC matrix converter with power controller for bidirectional inductive power transfer systems," *IEEE Trans. Ind. Appl.*, vol. 54, no. 4, pp. 3760–3770, Jul./Aug. 2018.
[16] N. X. Bac, D. M. Vilathgamuwa, and U. K. Madawala, "A matrix converter based inductive power transfer system," in *Proc. IEEE Conf. Power Energy*, Ho Chi Minh City, Vietnam, 2012, pp. 509–514.
[17] N. Xuan Bac, D. M. Vilathgamuwa, and U. K. Madawala, "A SiC-based matrix converter topology for inductive power transfer system," *IEEE Trans. Power Electron.*, vol. 29, no. 8, pp. 4029–4038, Aug. 2014.
[18] C. Li, Z. Wang, and Y. Xu, "A wireless-power-transfer-based three-phase PMSM drive system with matrix converter," *IEEE Trans. Ind. Electron.*, vol. 70, no. 3, pp. 2307–2317, Mar. 2023.
[19] Y. Hayashi, H. Motoyama, and T. Takeshita, "Wireless power transfer system using three-phase to single-phase matrix converter," in *Proc. Int. Conf. Power Electron.-ECCE Asia*, Niigata, Japan, 2018, pp. 356–362.
[20] Y. Xiao and C. Liu, "Direct load voltage control for electrolytic capacitorless wireless power transfer system without DC/DC converter," *IEEE Trans. Ind. Electron.*, vol. 68, no. 9, pp. 8039–8048, Sep. 2021.
[21] N. R. Mirković, D. M. Stojić, A. Delgado, P. Alou, and M. Vasić, "Novel three phase to single phase matrix converter modulation strategy for bidirectional inductive power transfer," *IEEE Trans. Power Electron.*, vol. 38, no. 12, pp. 14830–14846, Dec. 2023.
[22] Y. Wei, F. Wu, S. Wu, and H. Liu, "Improved modulation strategy for three-phase matrix converter-based WPT system," *IEEE Trans. Transp. Electr.*, vol. 10, no. 2, pp. 3396–3406, Jun. 2024.
[23] M. Moghaddami, A. Anzalchi, and A. I. Sarwat, "Single-stage three-phase AC-AC matrix converter for inductive power transfer systems," *IEEE Trans. Ind. Electron.*, vol. 63, no. 10, pp. 6613–6622, Oct. 2016.
[24] J. W. Kolar, T. Friedli, J. Rodriguez, and P. W. Wheeler, "Review of three-phase PWM AC-AC converter topologies," *IEEE Trans. Ind. Electron.*, vol. 58, no. 11, pp. 4988–5006, Nov. 2011.
[25] L. Empringham, J. W. Kolar, J. Rodriguez, P. W. Wheeler, and J. C. Clare, "Technological issues and industrial application of matrix converters: A review," *IEEE Trans. Ind. Electron.*, vol. 60, no. 10, pp. 4260–4271, Oct. 2013.
[26] *Wireless Power Transfer for Light-Duty Plug-In/Electric Vehicles and Alignment Methodology*, SAE J2954 Standard, SAE Int., Warrendale, PA, USA, Oct. 2020.
[27] G. He, Q. Chen, X. Ren, S. C. Wong, and Z. Zhang, "Modeling and design of contactless sliprings for rotary applications," *IEEE Trans. Ind. Electron.*, vol. 66, no. 5, pp. 4130–4140, May 2019.
[28] X. F. Chen, C. K. Tse, C. Jiang, and C. M. Lai, "Soft switching based design of a single-stage wireless DC motor drive system for typical mechanical loads," *IEEE Trans. Ind. Appl.*, vol. 60, no. 6, pp. 8976–8987, Nov./Dec. 2024.
[29] B. Wu and M. Narimani, *High-Power Converters and AC Drives*. Hoboken, NJ, USA: Wiley, 2017.
[30] *IEEE Standard for Interconnecting Distributed Resources with Electric Power Systems*, IEEE Standard 1547-2003, Jul. 2003.
[31] *IEEE Recommended Practice and Requirements for Harmonic Control in Electric Power Systems*, IEEE Std. 519-2014, Jun. 2014.
[32] WT500 power analyzer user's manual, Yokogawa Electric Corporation, Sep. 2019. [Online]. Available: https://cdn.tmi.yokogawa.com/1/5959/files/IM760201-01E.pdf
[33] J. Huber and J. W. Kolar, "Monolithic bidirectional power transistors," *IEEE Power Electron. Mag.*, vol. 10, no. 1, pp. 28–38, Mar. 2023.
[34] "NV6428 data sheet," Navitas Semiconductor, Mar. 2025. [Online]. Available: https://navitassemi.com/single-stage-bds/

Xin Felix Chen (Graduate Student Member, IEEE) received the B.S. and M.S. degrees in electrical engineering from the Nanjing University of Aeronautics and Astronautics, Nanjing, China, in 2016 and 2019, respectively. He is currently working toward the Ph.D. degree in electrical engineering with the City University of Hong Kong, Hong Kong, China.

His research interests include wireless motor drives and resonant converters.

Chi K. Tse (Fellow, IEEE) received the B.Eng. (first class hons.) and Ph.D. degrees in electrical engineering from the University of Melbourne, Melbourne, VIC, Australia, in 1987 and 1991, respectively.

He is currently an Associate Vice President of innovation, Director of Academy of innovation, and Chair Professor of electrical engineering with City University of Hong Kong, Hong Kong, China. His research interests include power electronics, nonlinear systems, and complex network applications.

Dr. Tse was the recipient of a number of research and invention prizes including the IEEE CASS Charles A. Desoer Technical Achievement Award, in 2022, and a few Best Paper Prizes from IEEE and other journals, as well as Gold Medal with Jury's Commendations and Grand Prizes in International Exhibition of Inventions of Geneva 2024, Asia Exhibition of Innovations and Inventions 2023, and Silicon Valley International Invention Festival 2019. He has been appointed to honorary professorship and distinguished fellowship by a few Australian, Canadian, and Chinese universities, including Chang Jiang Scholar Chair Professor with Huazhong University of Science and Technology, Honorary Professor of Melbourne University, and Distinguished Professor-at-Large with the University of Western Australia. He was the Panel Member of Hong Kong Research Grants Council, and a Member of several professional and government committees. In 2005, 2010, and 2018, he was selected as an IEEE Distinguished Lecturer. In 2006, he Chaired the IEEE CAS Technical Committee on Nonlinear Circuits and Systems. He serves and has served as the Editor-in-Chief for IEEE TRANSACTIONS ON CIRCUITS AND SYSTEMS II, from 2016 to 2019; IEEE CIRCUITS AND SYSTEMS MAGAZINE, from 2013 to 2016; IEICE Nonlinear Theory and Applications, since 2013; an Associate Editor of a few other IEEE journals; and on the Editorial Board of IEEE Proceedings, from 2021 to 2024. He has served on a number of IEEE committees including the IEEE Fellows Committee and the IEEE Awards Committee, and Chaired the Steering Committee of IEEE TRANSACTIONS ON NETWORK SCIENCE AND ENGINEERING.

C. Q. Jiang (Senior Member, IEEE) received the B.Eng. and M.Eng. degrees (first class hons.) in electrical engineering and automation from Wuhan University, Wuhan, China, in 2012 and 2015, respectively, and the Ph.D. degree in electrical and electronic engineering from The University of Hong Kong, Hong Kong, SAR, China, in 2019.

In 2019, he was a Visiting Researcher with Nanyang Technological University, Singapore. From 2019 to 2021, he was a Postdoctoral Research Associate with the University of Cambridge, Cambridge, U.K. Since 2021, he has been affiliated with Clare Hall, University of Cambridge, Cambridge, U.K. He is currently an Associate Professor with the Department of Electrical Engineering, and a Faculty Member with the State Key Laboratory of Terahertz and Millimeter Waves, City University of Hong Kong, Hong Kong, SAR, China. His research interests include power electronics, wireless power transfer, electric machines and drives, and electric vehicle technologies.

Dr. Jiang was the recipient of Y-LOT's Hong Kong SciTech Pioneers Award, Gold Medal with the Silicon Valley International Invention Festival, Gold Medals with Congratulations of the Jury in International Exhibition of Inventions of Geneva, Winner of CAPE Acorn Blue Sky Research Award at the University of Cambridge, Cambridge, U.K., and Gold Medal in 3 rd Asia Exhibition of Innovations and Inventions. Currently, he is an Associate Editor of IET Renewable Power Generation, and a Guest Editor for IEEE OPEN JOURNAL OF VEHICULAR TECHNOLOGY and IEEE TRANSACTIONS ON POWER ELECTRONICS LETTERS.

Qianhong Chen (Member, IEEE) received the B.S., M.S., and Ph.D. degrees in electrical engineering from the Nanjing University of Aeronautics and Astronautics (NUAA), Nanjing, China, in 1995, 1998, and 2001, respectively.

She is currently a Professor with the Department of Electrical Engineering, NUAA. Her research interests include application of integrated-magnetics, wireless power transfer, and high power density power converters.

Ching-Ming Lai (Senior Member, IEEE) received the Ph.D. degree in electrical engineering from the National Tsing Hua University, Taipei, Taiwan, in 2010.

From 2009 to 2012, he was a Senior Research and Development Engineer with Lite-On Technology Corporation, Taipei, Taiwan. From 2014 to 2019, he was a Faculty Member with the Department of Vehicle Engineering, National Taipei University of Technology (Taipei Tech), Taipei, Taiwan. Since 2019, he has been with the Department of Electrical Engineering, National Chung Hsing University (NCHU), Taichung, Taiwan. He is currently a Professor and the Director of the Intelligent Electric Vehicle and Green Energy Center, NCHU. His research interests include system integration, electric vehicles, power electronics, green energy technologies, and intelligent transportation.

Dr. Lai was the recipient of the 2008 Young Authors Award for Practical Application from the Society of Instrument and Control Engineers, Japan, Best Paper Award at the 2013 IEEE International Conference on Power Electronics and Drive Systems, Technical Award Paper of 2024 IEEE International Conference on Power Electronics Systems and Applications. He was the recipient of the Dr. Shechtman Youth Researcher Award from Taipei Tech, in 2018, Outstanding Youth Engineer Award from Chinese Institute of Engineers-Taichung Chapter, in 2020, and the Outstanding Engineering Professor from Chinese Institute of Engineers-Taichung Chapter, in 2024. In addition, according to Elsevier, since 2021, he has been listed in the World's Top 2% of Scientists (Field: Energy). Since 2024, he has been the Founder and Chair of the IEEE Systems Council Taipei Chapter. Besides, he serviced as the TPC Vice Chair of IEEE ECCE Asia-2025, General Chair of IEEE RASSE-2024, the Co-Chair of IEEE IFEEC-2021, the Tutorial Chair of IEEE IFEEC-2021, IEEEWiPDA-2019, and IEEE IFEEC-2015. Since 2017, he has been the Editor for IEEE TRANSACTIONS ON VEHICULAR TECHNOLOGY; and an Associate Editor for IEEE ACCESS, since 2021, and IEEE SYSTEMS JOURNAL, since 2025.